Journal of Engineering Mathematics **38:** 371–390, 2000.

A mathematical model of the edge-defined film-fed growth process

G. W. YOUNG and J. A. HEMINGER
Department of Mathematics and Computer Science, The University of Akron, Akron, Ohio 44325-4002, U.S.A.
e-mail: gwyoung@uakron.edu, jheminger@uakron.edu

Received 24 December 1997; accepted in revised form 13 July 1999

Abstract. A model is presented to simulate the steady-state growth of a fiber produced by the edge-defined film-fed growth (EFG) process. Equations describing the axisymmetric transport of heat in the melt and fiber are discussed. Heat transfer between the system and the surrounding environment is assumed to take place via convection and radiation. Given the fiber translation velocity, the external temperature profile, the die temperature, and the input flow rate or the pressure, asymptotic solutions for the temperature profiles in the melt and fiber, and the melt/gas and solidifying interfacial shapes are developed in the limit of a small melt slenderness ratio (fiber radius/approximate melt height). The effect of process parameters on the shape of the fiber system is investigated.

Key words: EFG process, fiber growth, asymptotic expansions, numerical simulation.

1. Introduction

Optical fibers have been used for many years for flexible light distribution bundles, faceplates for cathode-ray tubes, medical endoscopes, and similar purposes. Several different material systems are potentially useful for optical fiber preparation. These include compound silicate glass, doped and undoped high silicas, plastic-clad fibers, single material fibers, and liquid-core fibers. Due to its high melting point, there is current interest in using single crystal sapphire fibers for high-temperature fiber-optical applications, or as a fiber-reinforcing material for ceramic composites [1]. The total fabrication procedure for an optical fiber depends on the material system used. Since sapphire has a high melting point, the edge-defined film-fed fiber growth (EFG) process is selected. In this process, a sapphire fiber is grown by pulling it from the melt. The intent of this work is to develop and analyze a model of the EFG system.

The EFG system is shown schematically in Figure 1 (next page). The melt is pumped into a preheated die and a molten pool is formed above the upper surface of the die. A seed fiber is dipped into the melt to initiate the growing process. During drawing, the fiber is continuously cooled by the surrounding air as it moves away from the die at speed $\hat{V}$ (a $\hat{}$ denotes a dimensional quantity). The size of the molten zone is bounded by the upper surface of the die, the solidifying interface of the fiber ($\hat{H}(\hat{r}, \hat{t})$), and the liquid/gas interface of the melt ($\hat{R}(\hat{z}, \hat{t})$). The pool of melt is held in shape by capillary forces and gravity. This shape changes in response to the thermal fields and the rates at which the material is added and removed from the system. Thus, the solidifying surface and liquid/gas interface are free. The goal of the practitioner is to grow high-quality fibers with constant circular cross-section. Small fluctuations in the fiber diameter may lead to optical transmission loss or less than optimum yield strength. Further discussion on the EFG process may be found in [2–6].

In the EFG technique, smooth fiber pull rates, steady heat input, steady flow rates, and suppression of mechanical vibrations are necessary to steady the melt volume and location of

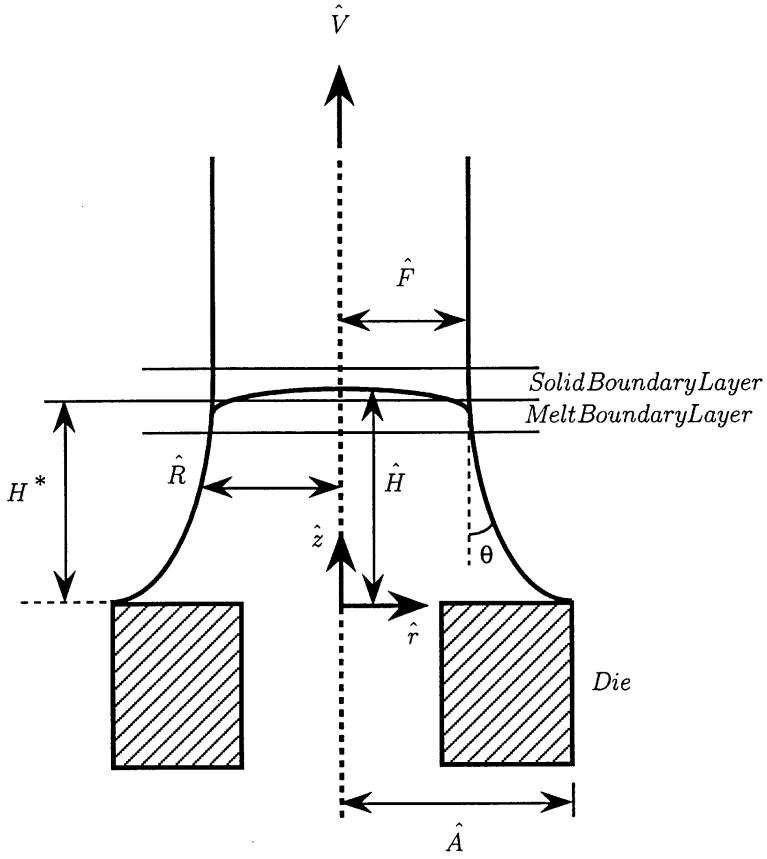

Figure 1. Schematic of the edge-defined film-fed fiber growth system.

the solidifying front. Fluctuations in these may lead to variations in the shape of the melt/gas interface, which in turn may lead to variations between the instantaneous contact angle θ, and its equilibrium value $\tilde{\theta}_0$, at the melt/fiber interface. The fiber responds by radially growing or shrinking at the solidification front to get back to the equilibrium value. As an initial step towards modelling this dynamic response, we present a steady-state analysis of the EFG system. These results may be used as the initial input for a time-dependent study.

A one-dimensional time-independent numerical simulation and related experimental results on the edge-defined film-fed fiber growth process have been presented by Backman, Wei, Filler, Irwin, and Collins [1]. Liang and Shyy [7] and Shyy, Liang, and Wei [8] extend these calculations to two dimensions. These works appear to be the only literature dealing with the shape of the liquid zone ahead of the solidified fiber (Ettouney, Brown and Kalejs [9], and Ettouney and Brown [10] consider the effects of the liquid zone on the EFG growth of thin silicon sheets), which is very important in diameter control. Several investigations studying a similar meniscus-controlled process in a different crystal growth geometry have appeared in recent years [11–17]. These models consider the intricate coupling between heat, mass, and momentum transport within the floating-zone system used in containerless refinement of doped semiconductor materials and binary alloys. The floating-zone system is similar to the EFG process. In the floating-zone system, a molten pool is formed by a circumferential heat source (laser, Gaussian heater, induction coil, etc.) along the axis of a cylindrical feed rod.

The pool is bounded by the melting surface of the feed rod, the solidifying surface of the fiber, and the melt/gas interface.

There have been several asymptotic analyses of the floating-zone system. Kuiken and Roksnoer [11] and Kuiken [12] used an expansion procedure based upon a small surface-heat-transfer parameter. Young and Chait [14, 15] followed the asymptotic procedure developed by Brattkus and Davis [18] for analyzing directional solidification systems. In this procedure, expansions in a small aspect ratio were developed and a boundary-layer analysis was used near the solidification front. This analysis also requires small surface heat transfer, and thus the procedures in [12–15, 18] are closely related.

Because of the similarity between the floating-zone system and the edge-defined film-fed fiber growing process, we propose to apply the asymptotic method in [14, 15] to the EFG process. The model is formulated in a cylindrical coordinate system with its center located at the middle of the orifice of the die, as shown in Figure 1. The approach is to reduce the steady-state, nonlinear, coupled set of partial differential equations, which governs the fiber-growing system, to a set of nonlinear coupled ordinary differential equations by asymptotic methods. We shall take the slenderness ratio

$$\varepsilon = \frac{\hat{F}}{\bar{H}}, \tag{1.1}$$

where $\hat{F}$ is the mean radius of the fiber and $\bar{H}$ is an approximate measure of the height of the melt zone, as the small parameter in our asymptotic expansions. We will define $\bar{H}$ shortly using a heat balance at the solidification front.

Clearly, the limit $\varepsilon \to 0$ cannot be physically realized. Stability analyses of the static shapes of isothermal cylindrical liquid columns [19, 20] and liquid drops captured between cylindrical rods [21–24] define bounds on the height of the liquid column. If the liquid zone is lengthened beyond those bounds, the zone fails due to a capillary instability. For example, a cylindrical melt column, with radius sufficiently small that gravity is unimportant, exhibits the static capillary instability if the melt height exceeds $2\pi\hat{F}$ [19, 20, 23]. Sachs and Surek [25] and Tatarchenko and Brener [26] examine capillary stability of non-isothermal EFG systems. In particular, Tatarchenko and Brener [26] use a one-dimensional model of heat transfer (similar to the leading-order temperature profile we develop), and investigate the stability of a growing rod. They find for $\hat{F} > \frac{1}{2}\hat{A}$, where $\hat{A}$ is the outer radius of the die, that the range of stable growth may be wider than that predicted by isothermal capillary stability. Hence, in the analysis to follow, the die and ambient temperatures are set so that $\bar{H}$ is large enough to keep ε small, but not so large that the actual melt height is sufficient for meniscus failure by pinch-off.

Fiber-growth processes are also susceptible to a draw-resonance instability when the winder speed $\hat{V}$ is sufficiently large. Isothermal [cf. 27–30] and non-isothermal [cf. 31–34] slender body analyses have determined the critical drawing conditions defining this tensile instability. The EFG process is characterized by relatively slow drawing velocities and regulated winder tension, so that this type of draw resonance instability is not an issue. We note that the one-dimensional thermal problem in the melt and fiber, defined by an energy balance on a cylindrical control volume in [31–33], is derived at leading order in the asymptotic analysis to follow. Further, Gupta and Schultz [34] use the same type of outer-problem asymptotic scheme, as proposed in our analysis, to derive systematically this one-dimensional thermal problem. However, one should not make further comparisons between EFG and the glass-

fiber drawing process examined in [31–34]. EFG leads to fiber growth by solidification phase change, whereas glass fibers form by crystallization due to a rapid increase in viscosity.

As a final comment, asymptotic procedures, such as that proposed in our analysis, which take advantage of the disparity in length scales to reduce a full set of governing equations and boundary conditions to a simplified set of equations, has been pioneered in the analysis of thin liquid films. For further discussion of thin liquid films, the interested reader is referred to the excellent review article by Oron, Davis, and Bankoff [35].

2. Derivation of model and nondimensionalization

We assume that the EFG system shown in Figure 1 is axisymmetric. The molten material is pumped into a preheated die and a fiber is grown by pulling it upward from the melt at the steady velocity $\hat{V}$. We neglect buoyancy and thermocapillary flows due to the small values of the Rayleigh and Marangoni numbers for these slender fiber systems [7]. We assume a uniform melt flow, with velocity $\hat{V}$. This is consistent for the analysis below, which leads to a melt column which is a circular cylinder at the leading order. The rate of change of the melt volume equals the difference of the input flow rate and the volume solidification rate. At steady state, these rates are equal. This mass balance sets the value of the fiber radius, so that $\hat{F} = \sqrt{Q/(\pi \hat{V})}$. Here, the density is assumed to be the same for both the melt and the solid, and Q is the volumetric flow rate of the input melt.

We nondimensionalize the governing equations by scaling the vertical coordinate $\hat{z}$ and the location of the solidifying front $\hat{z} = \hat{H}(\hat{r})$, with a representative measure $\bar{H}$ of the height of the melt. $\bar{H}$ is defined as

$$\bar{H} = \frac{k(\hat{T}_D - T_m)}{\frac{k_s(T_m - \hat{T}_\infty)}{\hat{L}^*} - L\hat{V}}, \tag{2.1}$$

where L is the latent heat per unit volume, k and k_s are the thermal conductivities in the liquid and the solid phases, T_m is the melting point of the fiber material, $\hat{T}_D$ is the temperature of the die, $\hat{T}_\infty$ is the far-field value of the imposed external temperature field, and $\hat{L}^*$ is the length of the fiber. Equation (2.1) is derived from the heat balance, Equation (2.7), at the solidification front, under the assumption of a planar front and using linear approximations for the temperature fields. This expression captures the basic trends that the melt height increases with increasing die temperature, increasing ambient temperature, and increasing pull rate. However, it does tend to overestimate the melt height, since it assumes perfect radial heat transfer across the system boundaries. The radial coordinate is scaled by $\hat{F}$, the radius of the fiber. The temperatures are scaled with the melting point T_m, of the fiber material. In the equations to follow, quantities without the $\hat{}$ are dimensionless.

The temperatures, T in the melt and T_S in the solidifying fiber, both satisfy the steady state heat equation,

Melt: $0 \leqslant z \leqslant H(r)$

$$\varepsilon^2 \,\mathrm{Pe}\frac{\partial T}{\partial z} = \frac{\partial^2 T}{\partial r^2} + \frac{1}{r}\frac{\partial T}{\partial r} + \varepsilon^2 \frac{\partial^2 T}{\partial z^2}. \tag{2.2}$$

Solid: $H(r) \leqslant z < \infty$

Table 1. Reference data for the sapphire material system.

Parameter	Value	Parameter	Value
Radius of the fiber $\hat{F}$	0·005 cm	Liquid phase thermal diffusivity κ	0.76 $cm^2\,s^{-1}$
z-coordinate length scale $\bar{H}$	0·067 cm	Liquid phase density ρ	3053 $kg\,m^{-3}$
Velocity of the fiber $\hat{V}$	0·0015 $cm\,s^{-1}$	Emissivity ε_m	0·4
Contact angle $\tilde{\theta}_0$	12°	Heat transfer coefficients h_L, h_S	5 $W°C^{-1}\,m^{-2}$
Melting point T_m	2596°K	Surface tension σ	0·665 $N\,m^{-1}$
Latent heat L	3190 $J\,cm^{-3}$	Die temperature $\hat{T}_D$	2636°K
Solid phase thermal conductivity k_S	2·6 $W°K^{-1}\,m^{-1}$	Outer radius of the die $\hat{A}$	0·008 cm
Liquid phase thermal conductivity k	4·2 $W°K^{-1}\,m^{-1}$	External temperature parameter a	4
Solid phase thermal diffusivity κ_S	0·011 $cm^2\,s^{-1}$	Far field temperature $\hat{T}_\infty$	26°C
		Input flow rate Q	$1{\cdot}18 \times 10^{-7}$ $cm^3\,s^{-1}$
		Fiber length $\hat{L}^*$	2·0 cm

$$\varepsilon^2 \,\mathrm{Pe_S} \frac{\partial T_S}{\partial z} = \frac{\partial^2 T_S}{\partial r^2} + \frac{1}{r}\frac{\partial T_S}{\partial r} + \varepsilon^2 \frac{\partial^2 T_S}{\partial z^2}. \tag{2.3}$$

Here

$$\varepsilon = \frac{\hat{F}}{\bar{H}}, \tag{2.4}$$

denotes the slenderness ratio of the melt column. Using the data listed in Table 1, we find that $\varepsilon = 0{\cdot}075$. Eventually, we shall seek solutions to the governing equations in the limit of small ε. We note that, since $\bar{H}$ overestimates the actual melt height, it is possible that $\varepsilon < 1/2\pi$, but the actual melt height is less than $2\pi\hat{F}$, so that the melt column is still stable. We also define the thermal Peclet numbers in the liquid zone and solid, $\mathrm{Pe} = \hat{V}\bar{H}/\kappa$ and $\mathrm{Pe_S} = \hat{V}\bar{H}/\kappa_S$, respectively. Here κ and κ_S denote the thermal diffusivities in the melt and solid.

We assume that the input melt is heated by the die and reaches the same temperature as the die, denoted by $\hat{T}_D$, when it is pumped into the liquid zone. We require that the liquid/gas interface, denoted by $\hat{R}(\hat{z})$, has a fixed contact line where it contacts the upper surface of the die. $\hat{A}$ is the outer radius of the die. $\hat{A}$ and $\hat{R}(\hat{z})$ are scaled by $\hat{F}$. Hence, at the upper surface of the die ($z = 0$), we impose the conditions

$$T = T_D, \qquad R(0) = A. \tag{2.5}$$

At the solidifying interface the temperatures of both liquid and solid are the same, namely the melting point T_m. The liquid/gas interface merges into the edge of the growing fiber ($\hat{r} = \hat{F}$) at $z = H(r)$. The solid fiber is assumed to be a cylinder of constant radius $\hat{F}$. Thus, at the solidifying interface ($z = H(r)$) we have

$$T = 1, \qquad T_S = 1, \qquad R(H) = 1. \tag{2.6}$$

The heat transfer between the melt and the solid at the solidifying interface is governed by

$$-\varepsilon^2 \,\mathrm{St}\,\mathrm{Pe} = K\left(\varepsilon^2\frac{\partial T_S}{\partial z} - \frac{\partial T_S}{\partial r}\frac{\mathrm{d}H}{\mathrm{d}r}\right) - \left(\varepsilon^2\frac{\partial T}{\partial z} - \frac{\partial T}{\partial r}\frac{\mathrm{d}H}{\mathrm{d}r}\right). \tag{2.7}$$

Here St is the Stefan number, $L/(\rho C_p T_m)$, and C_p is the heat capacity. Further, K is defined as k_s/k.

Above the solidifying interface, the fiber is cooled by the surrounding air and the fiber temperature eventually becomes the same as the far-field temperature $\hat{T}_\infty$, of the imposed external temperature $\hat{T}_a$. In reality $\hat{T}_a$ is determined by the interaction of a hot plume of gas that rises off the top surface of the die. Hence, it is more appropriate to solve a heat-transfer problem to determine the external temperature as a function of heat loss to the surrounding chamber, and heat transfer with the die. However, we simplify the analysis by assuming that $\hat{T}_a$ is known. Hence, we impose the following far-field condition as $z \to L^*$

$$T_S = T_\infty. \tag{2.8}$$

In the analysis to follow, L^* is assumed to be much larger than the height of the melt column.

Along the z-axis ($r = 0$), we impose the symmetry conditions

$$\frac{\partial T}{\partial r} = 0, \qquad \frac{\partial T_S}{\partial r} = 0. \tag{2.9}$$

At the melt/gas interface ($r = R(z)$), we have

$$\frac{-\frac{\partial T}{\partial r} + \varepsilon^2 \frac{\partial T}{\partial z}\frac{\mathrm{d}R}{\mathrm{d}z}}{\sqrt{1+\varepsilon^2\left(\frac{\mathrm{d}R}{\mathrm{d}z}\right)^2}} = B_L(T - T_a) + R_L(T^4 - T_a^4), \tag{2.10}$$

$$-P_B + \mathrm{Bo}\, z = \left[\frac{-1}{R\sqrt{1+\varepsilon^2\left(\frac{\mathrm{d}R}{\mathrm{d}z}\right)^2}} + \varepsilon^2 \frac{\frac{\mathrm{d}^2R}{\mathrm{d}z^2}}{\left[1+\varepsilon^2\left(\frac{\mathrm{d}R}{\mathrm{d}z}\right)^2\right]^{3/2}}\right]. \tag{2.11}$$

Equation (2.10) represents an energy balance for heat transfer between the melt and the surrounding air. Since temperatures are high, both convective and radiative heat losses are significant. The Biot number and the radiation number in the liquid phase are defined, respectively, as $B_L = h_L \hat{F}/k$ and $R_L = \sigma_B \varepsilon_m T_m^3 \hat{F}/k$. Here h_L, is the heat-transfer coefficient, σ_B is the Stefan–Boltzman constant and ε_m is the emissivity.

Equation (2.11) describes the normal force balance on the interface. Here, P_B is the unknown hydrodynamic fluid pressure (pressure is scaled by $\sigma/\hat{F}$) and $\mathrm{Bo} = \rho g \overline{H} \hat{F}/\sigma$ is the Bond number, where ρ is the melt density, g is gravity, and σ is surface tension. The Bond number is small due to the large value of the surface tension and small fiber radius (see Table 1). Hence, in the limit of small aspect ratio ε, small Bond number, uniform melt flow, and contact-line location A, near 1, Equation (2.11) will lead to a melt column which is a circular cylinder at leading order. This is why we define $R = 1 + f(z)$, where it is assumed that $f \ll 1$. Under this assumption, Equations (2.5b) and (2.6c) become

$$f(0) = A - 1, \qquad f(H) = 0. \tag{2.12}$$

Similar to the above discussion, we write the pressure as

$$P_B = P_{B0} + P_{B1}, \tag{2.13}$$

where we assume $P_{B1} \ll P_{B0}$. Further, we take the Bond number to be of the same size as f and P_{B1}. Using these assumptions, we derive from the normal force balance, Equation (2.11), that

$$P_{B0} = 1, \qquad -P_{B1} + \mathrm{Bo}\, z = f + \varepsilon^2 \frac{\mathrm{d}^2 f}{\mathrm{d}z^2}, \tag{2.14}$$

where P_{B0} is the pressure necessary to keep the melt column as a right circular cylinder with dimensionless radius 1, and P_{B1} is unknown.

Finally, along the solid boundary of the product fiber ($r = 1$), there is the energy balance

$$-\frac{\partial T_S}{\partial r} = B_S(T_S - T_a) + R_S(T_S^4 - T_a^4). \tag{2.15}$$

Here the Biot number B_S in the solid fiber is defined by $B_S = h_S \hat{F}/k_S$ and the radiation number R_S in the solid is defined by $R_S = \sigma_B \varepsilon_m T_m^3 \hat{F}/k_S$, where h_S is the heat-transfer coefficient in the solid fiber.

In the steady state, the contact angle θ between the liquid/gas interface and solid/gas interface, shown in Figure 1, remains fixed at its equilibrium value $\tilde{\theta}_0$. Since $\tilde{\theta}_0$ is on the order of 10 degrees, we pose $\tilde{\theta}_0$ to be of $O(\varepsilon)$, $\tilde{\theta}_0 = \varepsilon\theta_0$. This assumption on the contact angle is consistent with treating the melt column as a perturbation of a right circular cylinder. Hence, we impose the contact-angle condition

$$\frac{\mathrm{d}f}{\mathrm{d}z}(H) = -\theta_0. \tag{2.16}$$

Overall, for the EFG system shown in Figure 1, the governing equations for system heat transfer in the melt and fiber and for the locations of the free boundaries, $H(r)$ and $R(z)$ (or equivalently $f(z)$), are Equations (2.2) and (2.3), subject to the boundary conditions (2.5a), (2.6a,b), (2.8), and (2.9), along with the energy exchanges on the interfaces (2.7), (2.10), and (2.15), together with the equation for the shape of the liquid/gas interface, (2.14b), with the conditions (2.12) and (2.16).

3. Solution procedure

3.1. Outer solution

We are looking for an approximate solution to the governing system in the limit of small slenderness ratio ε. Assuming that $\varepsilon \ll 1$, we seek solutions for T_S and T in the following form

$$T = T_0 + \varepsilon T_1 + \varepsilon^2 T_2 + O(\varepsilon^3), \qquad T_S = T_{S0} + \varepsilon T_{S1} + \varepsilon^2 T_{S2} + O(\varepsilon^3). \tag{3.1}$$

By taking the surface-heat-transfer parameters, B_L and R_L, as $O(1)$ quantities, we find too much heat transfers into the system, in the sense that the temperature of the liquid zone is the same as that of the imposed external profile. Thus, as in Brattkus and Davis [18] and Young and Chait [14, 15], we pose that the radiation number and Biot number are $O(\varepsilon^2)$ quantities. We note for the data lised in Table 1 and by the estimates of Shyy, Liang, and Wei [8], that

these quantities are approximately $O(10^{-3})$. So we define $R_L = \varepsilon^2 \bar{R}_L$, $B_L = \varepsilon^2 \bar{B}_L$, and Equation (2.10) becomes

$$\frac{-\frac{\partial T}{\partial r} + \varepsilon^2 \frac{\partial T}{\partial z}\frac{\mathrm{d}R}{\mathrm{d}z}}{\sqrt{1+\varepsilon^2\left(\frac{\mathrm{d}R}{\mathrm{d}z}\right)^2}} = \varepsilon^2 \bar{B}_L(T - T_a) + \varepsilon^2 \bar{R}_L(T^4 - T_a^4). \tag{3.2}$$

This scaling balances the surface heat transfer with the axial diffusion of heat. These scalings are also consistent with the numerical solutions in [1, 7, 8] which indicate that the radial thermal gradients are low in comparison to the axial gradients. In summary, the above assumptions exploit geometrical (slender body) and physical (low radial heat transfer) attributes in order to simplify the analysis.

At $O(1)$, the solution to Equation (2.2) is

$$T_0 = d(z), \tag{3.3}$$

where $d(z)$ is unknown. At $O(\varepsilon)$ in the solution procedure we find that

$$T_1 = d_1(z), \tag{3.4}$$

where $d_1(z)$ is also unknown. Proceeding to the $O(\varepsilon^2)$ version of Equation (2.2), and using Equation (3.3), we find

$$\mathrm{Pe}\, d' = \frac{1}{r}\frac{\partial}{\partial r}\left(r\frac{\partial T_2}{\partial r}\right) + d''. \tag{3.5}$$

In the above the prime mark ($'$) denotes differentiation with respect to z. Upon integration, we find that

$$T_2 = (\mathrm{Pe}\, d' - d'')\frac{r^2}{4} + d_2(z), \tag{3.6}$$

where $d_2(z)$ is another unknown function of integration. We note that Equations (3.1a), (3.3, 3.4), and (3.6) lead to a parabolic profile for the temperature isotherms, which is similar to the numerical simulation predictions of Liang and Shyy [7] and Shyy, Liang, and Wei [8]. The $O(\varepsilon^2)$ version of Equation (3.2) is

$$-\frac{\partial T_2}{\partial r} + d'R' = \bar{B}_L(d - T_a) + \bar{R}_L(d^4 - T_a^4). \tag{3.7}$$

Substituting Equation (3.6) in Equation (3.7), we find a differential equation for $d(z)$,

$$-\frac{R}{2}(\mathrm{Pe}\, d' - d'') + d'R' = \bar{B}_L(d - T_a) + \bar{R}_L(d^4 - T_a^4). \tag{3.8}$$

By solving Equation (3.8) subject to the boundary conditions (2.5a) and (2.6a), we can find an approximate solution for the temperature of the melt zone. We note that, if the Biot and radiation numbers are large in Equation (3.8), the leading-order temperature profile in the melt will equal the ambient profile, as discussed earlier.

For the temperature of the solidified fiber, we follow the same solution procedure. We scale the radiation number and Biot number by ε^2, via $R_S = \varepsilon^2 \bar{R}_S$, $B_S = \varepsilon^2 \bar{B}_S$, and use the $O(\varepsilon^2)$ version of Equation (2.3) to find that

$$T_{S2} = (\mathrm{Pe_S}\, d_S' - d_S'')\frac{r^2}{4} + d_{S2}(z), \tag{3.9}$$

where $T_{S0} = d_S(z)$ and $d_{S2}(z)$ are unknown. Finally, substituting Equation (3.9) in the $O(\varepsilon^2)$ version of Equation (2.15), we find the differential equation for the leading-order solution of the fiber temperature field $d_S(z)$

$$-\tfrac{1}{2}(\mathrm{Pe_S}\, d_S' - d_S'') = \bar{B}_S(d_S - T_a) + \bar{R}_S(d_S^4 - T_a^4). \tag{3.10}$$

Equation (3.10) is subject to the boundary conditions (2.6b) and (2.8).

In summary, by means of an asymptotic procedure, we find differential equations, viz. Equations (3.8) and (3.10), for the temperature fields in both the melt zone and the solid fiber. The solutions of Equations (3.8, 3.10) provide the leading-order temperature profiles. These one-dimensional approximations will be valid, provided that the radially dependent correction terms in Equations (3.6, 3.9) are small in comparison to these approximations. The coefficients of the radially dependent terms in Equations (3.6, 3.9) are related to the right-hand-side terms in Equations (3.8, 3.10), provided that the meniscus tapering is not so steep that the $d'R'$ is significant in Equation (3.8). Hence, it can be shown that the radially dependent correction terms are small, in comparison to the leading-order one-dimensional temperature fields, provided that $(B_i(d_i - T_a) + R_i(d_i^4 - T_a^4))/(2d_i) \ll 1$, $i = L, S$, which means that the radial heat transfer is small in Equations (2.10, 2.15). In deriving the above, we have used the original definitions of the Biot and radiation numbers. In our scaling scheme, the d_i and T_a are approximately 1. Hence, the one-dimensional approximations are valid for $B_i + R_i \ll 2$.

3.2. Boundary-layer solution

The inner problem deals with the area close to the solidifying interface. Because of the small radial thermal gradients, we pose that this interface can be represented as

$$H(r) = H^* + \varepsilon^2 h(r), \tag{3.11}$$

where H^* is the mean position of the solidifying interface, as shown in Figure 1, and $h(r)$ is the nonplanar correction to this liquid/solid interfacial shape. Both H^* and $h(r)$ are unknown. At this interface, we have not yet satisfied the latent-heat Equation (2.7). At this point, one could substitute the leading-order temperature fields in Equation (2.7) and develop coupled equations for the mean interface location H^*. However, to determine the nonplanar correction, $h(r)$ requires a boundary layer analysis. Following Brattkus and Davis [18] and Young and Chait [14, 15], we construct a solid boundary layer and a melt boundary layer just above and below H^*. We introduce the boundary-layer coordinate

$$\eta = \frac{z - H^*}{\varepsilon}, \tag{3.12}$$

so that η is 0 at the mean location of the solidifying front, and away from the solidifying front, $\eta \to \infty$ into the fiber and $\eta \to -\infty$ into the melt. For the inner problem, we write the temperatures of the melt and the solidifying fiber as

$$\bar{T} = \bar{T}_0 + \varepsilon\bar{T}_1 + \varepsilon^2\bar{T}_2 + O(\varepsilon^2), \qquad \bar{T}_S = \bar{T}_{S0} + \varepsilon\bar{T}_{S1} + \varepsilon^2\bar{T}_{S2} + O(\varepsilon^2), \tag{3.13}$$

respectively. We also expand $h(r)$ as

$$h(r) = h_0(r) + \varepsilon h_1(r) + \varepsilon^2 h_2(r) + O(\varepsilon^3). \tag{3.14}$$

Our goal is to find h_0, the leading-order solution of the correction. Using the change of variables defined by Equation (3.12), we determine the melt inner problem

$$\frac{\partial^2 \bar{T}}{\partial r^2} + \frac{1}{r}\frac{\partial \bar{T}}{\partial r} + \frac{\partial^2 \bar{T}}{\partial \eta^2} = \varepsilon \,\mathrm{Pe_S} \frac{\partial \bar{T}}{\partial \eta}. \tag{3.15}$$

while the fiber inner problem is

$$\frac{\partial^2 \bar{T}_S}{\partial r^2} + \frac{1}{r}\frac{\partial \bar{T}_S}{\partial r} + \frac{\partial^2 \bar{T}_S}{\partial \eta^2} = \varepsilon \,\mathrm{Pe_S} \frac{\partial \bar{T}_S}{\partial \eta}. \tag{3.16}$$

The conditions at the solidifying interface, $\eta = \varepsilon h(r)$, Equations (2.6a, b) and (2.7), become

$$\bar{T} = 1, \qquad \bar{T}_S = 1, \tag{3.17}$$

$$-\varepsilon \,\mathrm{St\,Pe} = K\left(\frac{\partial \bar{T}_S}{\partial \eta} - \varepsilon \frac{\partial \bar{T}_S}{\partial r}\frac{\mathrm{d}h}{\mathrm{d}r}\right) - \left(\frac{\partial \bar{T}}{\partial \eta} - \varepsilon \frac{\partial \bar{T}}{\partial r}\frac{\mathrm{d}h}{\mathrm{d}r}\right). \tag{3.18}$$

We also change variables for the boundary conditions, Equations (2.10) and (2.15) at the liquid/gas interface and the solid/gas interface. These become, respectively

$$\frac{-\frac{\partial \bar{T}}{\partial r} + \frac{\partial \bar{T}}{\partial \eta}\frac{\mathrm{d}R}{\mathrm{d}\eta}}{\sqrt{1 + \left(\frac{\mathrm{d}R}{\mathrm{d}\eta}\right)^2}} = \varepsilon^2 \bar{B}_L(\bar{T} - T_a) + \varepsilon^2 \bar{R}_L(\bar{T}^4 - T_a^4), \tag{3.19}$$

$$-\frac{\partial \bar{T}_S}{\partial r} = \varepsilon^2 \bar{B}_S(\bar{T}_S - T_a) + \varepsilon^2 \bar{R}_S(\bar{T}_S^4 - T_a^4). \tag{3.20}$$

To complete the boundary-layer problem, we impose the matching conditions. For the melt region, we have

$$\lim_{\eta \to -\infty} (T - \bar{T}) = 0. \tag{3.21}$$

The outer solution is determined by Equations (3.1a), (3.3, 3.4), and (3.6). Substituting these in Equation (3.21), we find

$$\begin{aligned}\lim_{n \to -\infty} \Bigg\{ \Bigg[& \left(T_0(H^*) + \frac{\partial T_0}{\partial z}(H^*)\varepsilon\eta + \frac{1}{2!}\frac{\partial^2 \bar{T}_0}{\partial z^2}(H^*)\varepsilon^2\eta^2 + \cdots \right) \\ & + \left(\varepsilon T_1(H^*) + \varepsilon \frac{\partial T_1}{\partial z}(H^*)\varepsilon\eta + \cdots \right) \\ & + \varepsilon^2 \left(P_e \frac{\partial T_0}{\partial z}(H^*) - \frac{\partial^2 \bar{T}_0}{\partial z^2}(H^*) \right) \frac{r^2}{4} + \varepsilon^2 d_2(H^*) + \cdots \Bigg] \\ & + \cdots - \left(\bar{T}_0 + \varepsilon \bar{T}_1 + \varepsilon^2 \bar{T}_2 + \cdots \right) \Bigg\} = 0. \end{aligned} \tag{3.22}$$

From here, one can determine the matching conditions at various orders. A similar procedure is used for matching in the fiber system.

The leading-order problems in the melt and fiber lead to

$$\bar{T}_0(r,\eta) = 1, \qquad \bar{T}_{S0}(r,\eta) = 1. \tag{3.23}$$

By matching the $O(1)$ terms, we find that

$$T_0(H^*) = d(H^*) = 1, \qquad T_{S0}(H^*) = d_S(H^*) = 1. \tag{3.24}$$

At order $O(\varepsilon)$, we find that

$$\bar{T}_1(r,\eta) = \frac{\partial T_0}{\partial z}(H^*)\eta, \qquad \bar{T}_{S1}(r,\eta) = \frac{\partial T_{S0}}{\partial z}(H^*)\eta. \tag{3.25}$$

We also find the $O(\varepsilon)$ version of Equation (3.18)

$$K\frac{\partial T_{S0}}{\partial z}(H^*) - \frac{\partial T_0}{\partial z}(H^*) = -\mathrm{St}\,\mathrm{Pe}, \tag{3.26}$$

which determines the location H^*, after solving Equations (3.8) and (3.10).

To find the first nonplanar correction h_0, to the shape of the solidifying interface, we find that we must solve for $\bar{T}_2$ and $\bar{T}_{S2}$. To accomplish this, we introduce the modified temperatures J_2 and J_{S2}, such that

$$\bar{T}_2 = J_2 + \left(\mathrm{Pe}\frac{\partial T_0}{\partial z}(H^*) - \frac{\partial^2 T_0}{\partial z^2}(H^*)\right)\frac{r^2}{4} + d_2(H^*) + \frac{\partial T_1}{\partial z}(H^*)\eta + \frac{1}{2}\frac{\partial^2 T_0}{\partial z^2}(H^*)\eta^2, \tag{3.27}$$

$$\bar{T}_{S2} = J_{S2} + \left(\mathrm{Pe_S}\frac{\partial T_{S0}}{\partial z}(H^*) - \frac{\partial^2 T_{S0}}{\partial z^2}(H^*)\right)\frac{r^2}{4} + d_{S2}(H^*) + \frac{\partial T_{S1}}{\partial z}(H^*)\eta + \frac{1}{2}\frac{\partial^2 T_{S0}}{\partial z^2}(H^*)\eta^2. \tag{3.28}$$

After substituting Equations (3.27) and (3.28) in the $O(\varepsilon^2)$ versions of Equations (3.15) and (3.16), we find

$$\frac{\partial^2 J_2}{\partial r^2} + \frac{1}{r}\frac{\partial J_2}{\partial r} + \frac{\partial^2 J_2}{\partial \eta^2} = 0, \tag{3.29}$$

$$\frac{\partial^2 J_{S2}}{\partial r^2} + \frac{1}{r}\frac{\partial J_{S2}}{\partial r} + \frac{\partial^2 J_{S2}}{\partial \eta^2} = 0. \tag{3.30}$$

We repeat this with the boundary conditions. Equations (2.9) and (3.18) give

$$\frac{\partial J_2}{\partial r} = \frac{\partial J_{S2}}{\partial r} = 0, \quad (r = 0), \tag{3.31}$$

$$K\frac{\partial J_{S2}}{\partial \eta} - \frac{\partial J_2}{\partial \eta} = 0, \quad (\eta = 0). \tag{3.32}$$

The boundary conditions (3.19) and (3.20) at $O(\varepsilon^2)$ yield

$$\frac{\partial J_2}{\partial \eta} = \frac{\partial J_{S2}}{\partial r} = 0, \quad (r = 1). \tag{3.33}$$

The matching conditions are

$$\lim_{\eta \to -\infty} J_2 = 0, \qquad \lim_{\eta \to \infty} J_{S2} = 0. \tag{3.34}$$

The simplicity of these matching conditions motivates the change of variables defined by Equations (3.27) and (3.28). Finally, Equations (3.17a,b) are transformed into the following, which are valid at $\eta = 0$

$$J_2(H^*) - [\bar{B}_L(T_0 - T_a) + \bar{R}_L(T_0^4 - T_a^4)]\frac{r^2}{2} + d_2(H^*) + \frac{\partial T_0}{\partial z}(H^*)h_0(r) = 0, \tag{3.35}$$

$$J_{S2}(H^*) - [\bar{B}_S(T_{S0} - T_a) + \bar{R}_S(T_{S0}^4 - T_a^4)]\frac{r^2}{2} + d_{S2}(H^*) + \frac{\partial T_{S0}}{\partial z}(H^*)h_0(r) = 0. \tag{3.36}$$

We have used Equations (3.8) and (3.10) to arrive at these expressions.

To solve the above, we first make use of the definition of H^* as the mean position of the solidifying interface. Hence, from Equation (3.11)

$$\int_0^1 h_0 r \, \mathrm{d}r = 0. \tag{3.37}$$

Next, by integrating Equations (3.29) and (3.30) with respect to r from 0 to 1, and using the conditions (3.34a,b), we find that

$$\int_0^1 J_2 r \, \mathrm{d}r = 0, \qquad \int_0^1 J_{S2} r \, \mathrm{d}r = 0. \tag{3.38}$$

Equations (3.37) and (3.38a,b) will be used during the final search for $h_0(r)$.

Now, we solve Equations (3.29) and (3.30) by separation of variables. After applying boundary conditions, the solutions can be expressed as

$$J_{S2} = \sum_{i=1}^{\infty} a_i J_0(\sqrt{\lambda_i} r)\, \mathrm{e}^{-\sqrt{\lambda_i}\eta}, \tag{3.39}$$

$$J_2 = \sum_{i=1}^{\infty} b_i J_0(\sqrt{\lambda_i} r)\, \mathrm{e}^{\sqrt{\lambda_i}\eta}, \tag{3.40}$$

where J_0 denotes the Bessel function of the first kind, and λ_i are the zeros of the Bessel function J_1. After applying condition (3.32), we find that

$$Ka_i + b_i = 0, \tag{3.41}$$

for all i. This expression, together with Equations (3.35) and (3.36), are used to find a_i, b_i and $h_0(r)$.

Next, Equations (3.35) and (3.36) are multiplied by r and integrated with respect to r from 0 to 1. Making use of Equations (3.37) and (3.38), we find that

$$d_2(H^*) = \tfrac{1}{4}[\bar{B}_L(T_0 - T_a) + \bar{R}_L(T_0^4 - T_a^4)], \tag{3.42}$$

$$d_{S2}(H^*) = \tfrac{1}{4}[\bar{B}_S(T_{S0} - T_a) + \bar{R}_S(T_{S0}^4 - T_a^4)]. \tag{3.43}$$

Finally, we use conditions (3.35), (3.36), and (3.39–3.43), to find the leading part of the solution h_0, of the correction to the melt/solid solidifying interface

$$h_0(r) = \frac{K[\bar{B}_s(T_{S0} - T_a) + \bar{R}_S(T_{S0}^4 - T_a^4)] + [\bar{B}_L(T_0 - T_a) + \bar{R}_L(T_0^4 - T_a^4)]}{2\left[K\frac{\partial T_{S0}}{\partial z}(H^*) + \frac{\partial T_0}{\partial z}(H^*)\right]}(r^2 - \tfrac{1}{2}), \tag{3.44}$$

where the T_0 and T_{S0} terms are all evaluated at $z = H^*$. Here, both of these temperatures equal that of the melting point. The numerator of Equation (3.44) represents the radial surface heat transfer near the solidifying front, while the denominator corresponds to axial heat transfer near this front. The denominator is a negative quantity under the operating conditions we examine. The sign of the numerator is positive when the solidifying interface is located in a region where the ambient temperature is less than the melting point. Thus, the interface will be parabolic and concave-down under these processing conditions. This is the case for the operating conditions listed in Table 1. This also agrees with the numerical simulations in [7, 8]. Finally, we desire a planar interface in order to minimize thermal stresses caused by radial temperature gradients or to minimize solute segregation in multi-component melts with negligible convective flows parallel to the interface. This requires operating conditions which will minimize radial heat transfer at the front, or maximize the sum of the axial temperature gradients between the liquid and solid phases at this location.

4. Results

First we determine the shape of the melt/gas interface $R(z)$. We solve Equation (2.14b) subject to the conditions (2.12a,b) and (2.16), to find that

$$\begin{aligned} R(z) \;=\; & 1 - P_{B1} + \mathrm{Bo}\, z + \left[-\theta_0 - \mathrm{Bo} + \frac{P_{B1} + A - 1}{\varepsilon}\sin\left(\frac{H^*}{\varepsilon}\right)\right]\frac{\varepsilon}{\cos\left(\frac{H^*}{\varepsilon}\right)}\sin\left(\frac{z}{\varepsilon}\right) \\ & + (P_{B1} + A - 1)\cos\left(\frac{z}{\varepsilon}\right), \end{aligned} \tag{4.1}$$

where

$$P_{B1} = \frac{\mathrm{Bo}\, H^* \cos\left(\frac{H^*}{\varepsilon}\right) - \varepsilon(\theta_0 + \mathrm{Bo})\sin\left(\frac{H^*}{\varepsilon}\right) + A - 1}{\cos\left(\frac{H^*}{\varepsilon}\right) - 1}. \tag{4.2}$$

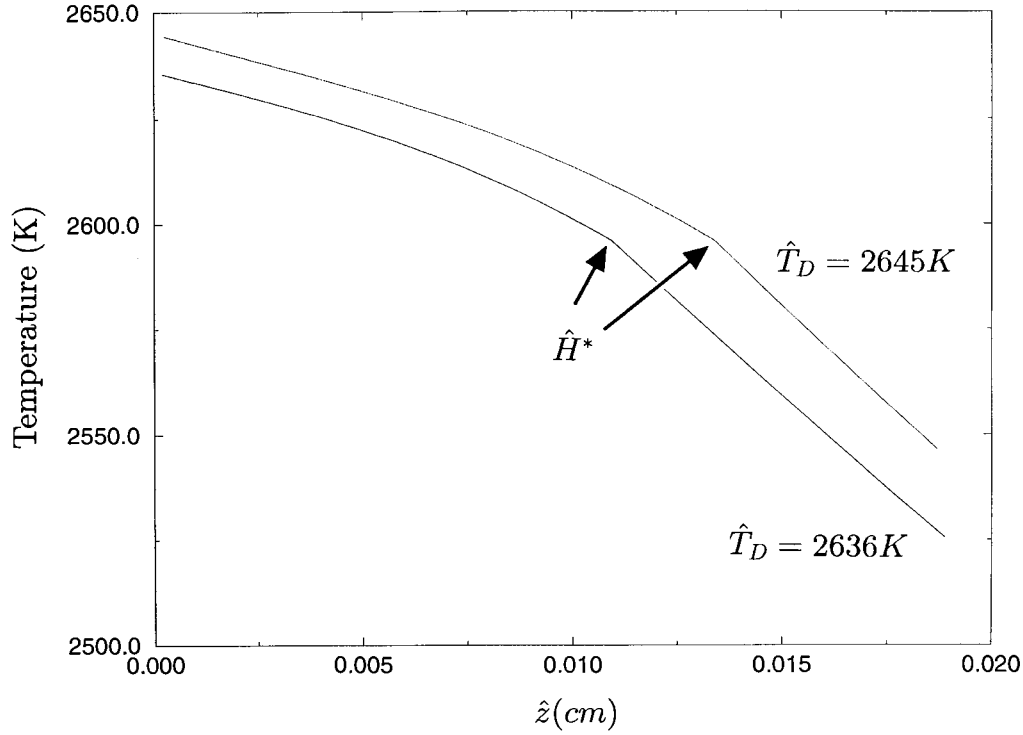

Figure 2. Temperature profiles in the melt ($0 \leqslant \hat{z} \leqslant H^*$) and fiber ($\hat{z} \geqslant H^*$) for two values of the die temperature $\hat{T}_D$.

The temperature in the melt satisfies Equation (3.8), subject to conditions (2.5a) and (2.6a). The temperature in the solid fiber satisfies Equation (3.10), subject to conditions (2.6b) and (2.8). However, Equations (2.6a,b) depend upon the mean position H^*, which is still unknown. Equation (3.26), which describes the relationship between the gradients of both temperatures at the solidifying interface, completes the definition of the problem.

Finite-difference methods are used to find the temperature distributions and the gradients for a given value of H^*. The boundary-value problems for the temperatures in the melt and fiber are each discretized by use of a fourth-order scheme. We solve the resulting nonlinear equations using Newton's method, where for each iteration the banded linear system is solved by use of the LINPACK subroutine DGBCO. These temperatures are then used to calculate the two one-sided derivatives of the temperatures at H^* by means of a fourth-order finite-difference approximation. These derivatives are substituted in Equation (3.26), to determine if a solution has been found. A direct search on H^* is performed until Equation (3.26) is satisfied.

The above procedure requires us to input the external temperature profile $T_a(z)$. We do not have laboratory data for this profile. If we choose T_a too large, the size of the melt zone will increase until the melt column becomes unstable and collapses. If we choose T_a too small, the melt will completely freeze. We choose the ambient temperature profile to have the form

$$T_a(z) = T_\infty + \frac{T_D - T_\infty}{\frac{z}{a} + 1}, \tag{4.3}$$

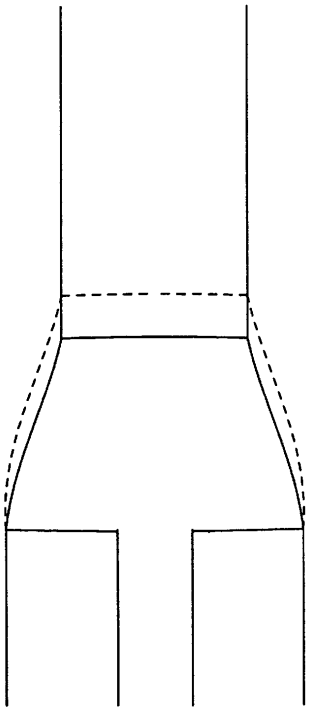

Figure 3. EFG system shapes corresponding to the temperature profiles shown in Figure 2 (solid) $\hat{T}_D = 2636\,\mathrm{K}$, (dashed) $\hat{T}_D = 2645\,\mathrm{K}$.

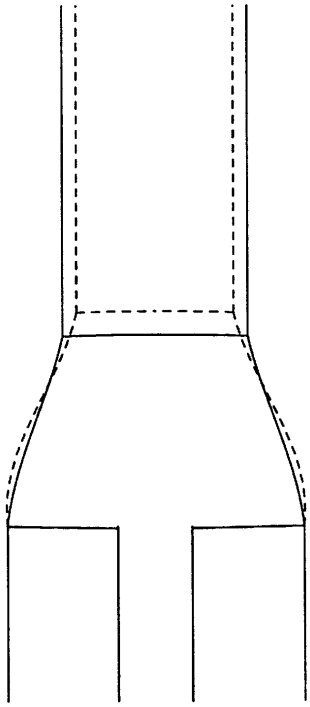

Figure 4. EFG system shapes for flow rates (solid) $Q = 1{\cdot}18 \times 10^{-7}\,\mathrm{cm}^3\,\mathrm{s}^{-1}$ and (dashed) $Q = 8{\cdot}5 \times 10^{-8}\,\mathrm{cm}^3/\mathrm{s}^{-1}$.

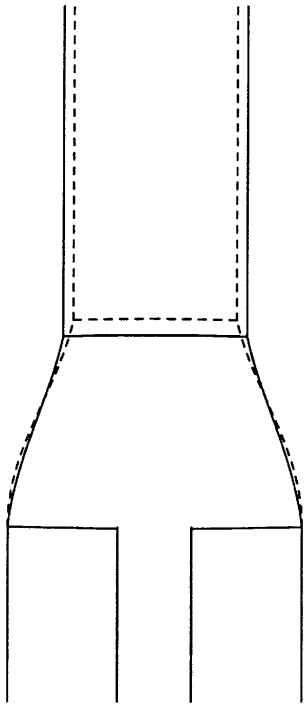

Figure 5. EFG system shapes for fiber pull rates (solid) $\hat{V} = 0{\cdot}0015\,\mathrm{cm\,s}^{-1}$ and (dashed) $\hat{V} = 0{\cdot}0019\,\mathrm{cm\,s}^{-1}$.

where T_∞ is the scaled far-field temperature, and a is a measure of the extent by which the external gas is heated by the surface of the die. Here T_D is the scaled temperature of the die. If the temperature of the die is changed, the height and the temperature distribution of the melt zone will also change. Figure 2 depicts this situation for different values of T_D, and for the data listed in Table 1. As expected, larger values of T_D lead to a longer melt column (a larger value of H^*). The same holds if a is increased.

We can now examine the shape of the EFG fiber-growth system for various parametric configurations. Given the flow rate and fiber pull rate, the radius of the fiber is set by $\hat{F} = \sqrt{Q/(\pi \hat{V})}$. The shape of the melt/gas interface is represented by Equation (4.1). Finally, the shape of the solidifying interface is given by Equations (3.11) and (3.44). The system shape for different die temperatures, as in Figure 2, is shown in Figure 3. The front curvature is slightly concave-down, as discussed previously. The flatness of the front profile is consistent with the numerical simulations presented in [7, 8].

As the volumetric flow rate Q, of the input melt decreases with all other conditions fixed, the radius of the fiber decreases. The length of the melt column lengthens, as shown in Figure 4, because the fixed ambient temperature profile acts upon a thinner fiber. Smaller values of $\hat{F}$ lead to lower radial heat transfer parameters, *i.e.* small Biot and radiation numbers. Hence, the melt cools more slowly, leading to a longer zone.

In Figure 5, we examine the effects of increasing the fiber pull velocity. The fiber becomes thinner and the height of the liquid zone increases.

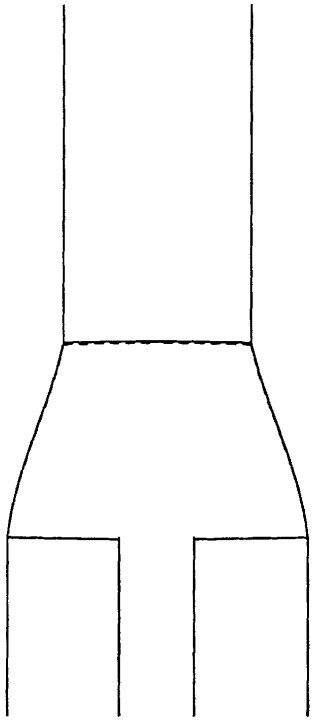

Figure 6. EFG system shapes for (solid) $Q = 1{\cdot}18 \times 10^{-7}$ $\mathrm{cm}^3\,\mathrm{s}^{-1}$, $\hat{V} = 0{\cdot}0015\,\mathrm{cm\,s}^{-1}$ and (dashed) $Q = 5{\cdot}9 \times 10^{-8}$ $\mathrm{cm}^3\,\mathrm{s}^{-1}$, $\hat{V} = 0{\cdot}00075\,\mathrm{cm\,s}^{-1}$.

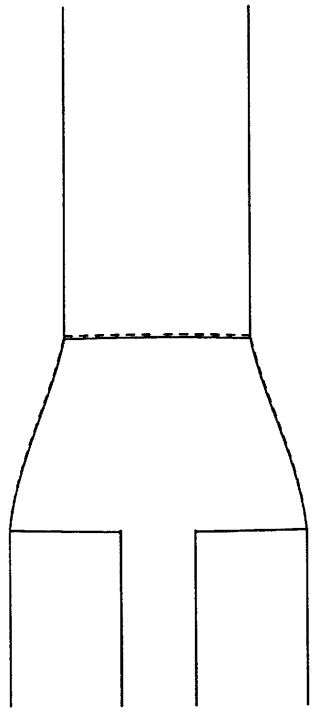

Figure 7. EFG system shapes for (solid) $Q = 1{\cdot}18 \times 10^{-7}\,\mathrm{cm}^3$ s^{-1}, $\hat{V} = 0{\cdot}0015\,\mathrm{cm\,s}^{-1}$ and (dashed) $Q = 2{\cdot}2125 \times 10^{-7}$ $\mathrm{cm}^3\,\mathrm{s}^{-1}$, $\hat{V} = 0{\cdot}0028125\,\mathrm{cm}$ s^{-1}.

Next, we decrease both Q and the drawing velocity $\hat{V}$ at the same rate, so that the fiber radius will be fixed. This situation is shown in Figure 6. As noted above, the location of H^* increases with decreasing flow rate, and decreases with decreasing pull velocity. These two effects appear to cancel each other, leaving H^* in approximately the same location. The slight decrease in location is due to the release of less latent heat with the slower velocity. Hence, the melt is slightly cooler.

Figure 7 is similar to the situation shown in Figure 6, although in this case both Q and $\hat{V}$ have been increased at the same rate.

5. Alternative configuration

In the processing configuration discussed above, the input flow rate Q is known and the pressure P_{B1} adjusts to satisfy the meniscus problem (2.14b), subject to (2.12) and (2.16). The fiber radius $\hat{F}$ is also determined by $\sqrt{Q/(\pi\hat{V})}$. Further, the analysis we have presented requires that the outer die radius $\hat{A}$ be close to $\hat{F}$ in magnitude, so that the leading-order melt column is a circular cylinder.

An alternative processing configuration is to drive the flow by capillary action [3, 9, 10, 26]. In this configuration, the hydrostatic pressure P_{B1}, is known, since one knows the distance

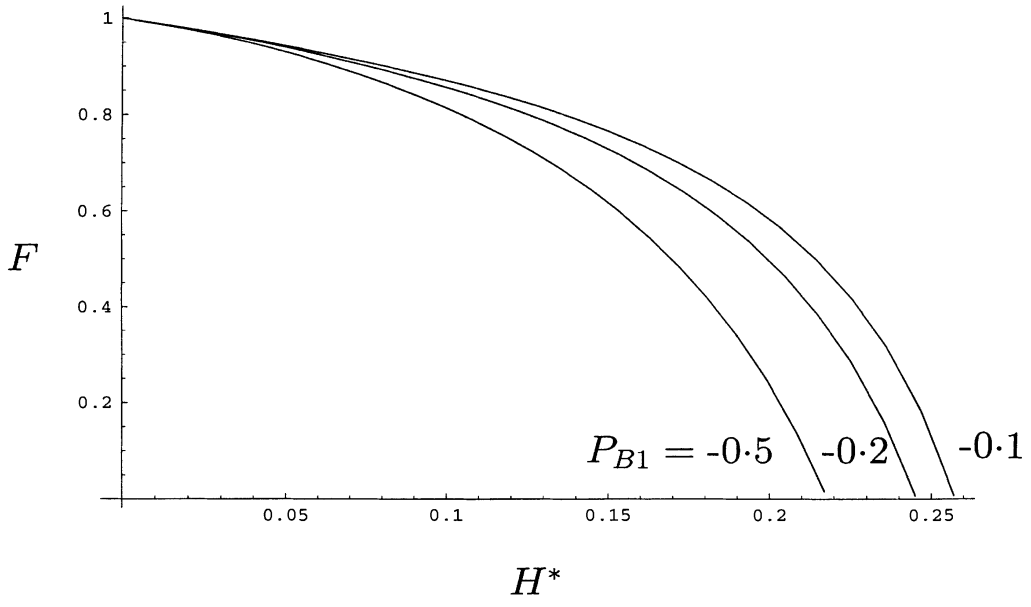

Figure 8. Variation of the fiber radius with pressure P_{B1} and melt height H^*.

between the top of the die surface and the liquid pool which supplies the melt. In this case, the fiber radius is not predetermined, but adjusts so that the meniscus problem is satisfied. To model this configuration, we make a few modifications to the previous analysis. We now scale the radial coordinate with the outer die radius $\hat{A}$, rather than the unknown $\hat{F}$. Appropriate modifications are made in the definition of the pressure scale, Bond, Biot, and radiation numbers. The only other modifications occur in the boundary conditions (2.12a, b). These become

$$f(0) = 0, \qquad f(H) = F - 1, \tag{5.1}$$

where F is the nondimensional version of the unknown fiber radius. In the case that F is close to 1, we again have a leading-order melt column which is a circular cylinder. We now solve the meniscus problem (2.14b), subject to (5.1) and (2.16). The solution is

$$R(z) = 1 - P_{B1} + \mathrm{Bo}\, z + \left[-\theta_0 - \mathrm{Bo} + \frac{P_{B1}}{\varepsilon}\sin\left(\frac{H^*}{\varepsilon}\right)\right]\frac{\varepsilon}{\cos\left(\frac{H^*}{\varepsilon}\right)}\sin\left(\frac{z}{\varepsilon}\right) + P_{B1}\cos\left(\frac{z}{\varepsilon}\right), \tag{5.2}$$

$$F = 1 - P_{B1} + \mathrm{Bo}\, H^* + \frac{P_{B1}}{\cos\left(\frac{H^*}{\varepsilon}\right)} - [\theta_0 + \mathrm{Bo}]\,\frac{\varepsilon \sin\left(\frac{H^*}{\varepsilon}\right)}{\cos\left(\frac{H^*}{\varepsilon}\right)}. \tag{5.3}$$

Figure 8 is a plot of Equation (5.3). In Equation (5.3), we see that the fiber radius is a function of the pressure. For $P_{B1} < 0$, the presure in the melt is less than that needed to sustain the cylindrical melt column. Hence, the meniscus bows inward and the contact angle decreases below the equilibrium value. Consequently, F decreases to compensate. Further, F

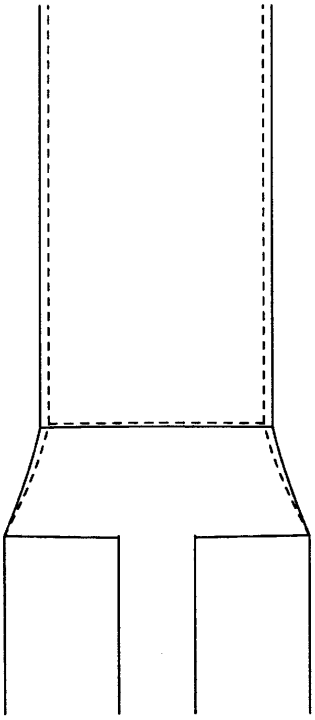

Figure 9. EFG system shapes for pressures (solid) $P_{B1} = -0{\cdot}1$ and (dashed) $P_{B1} = -0{\cdot}2$.

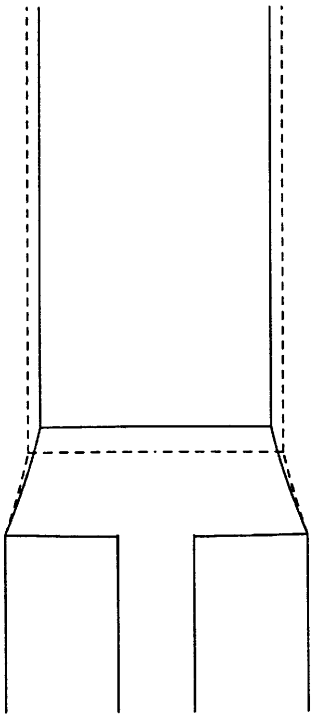

Figure 10. EFG system shapes for die temperatures (solid) $\hat{T}_D =$ 2620 K, (dashed) $\hat{T}_D = 2615$ K.

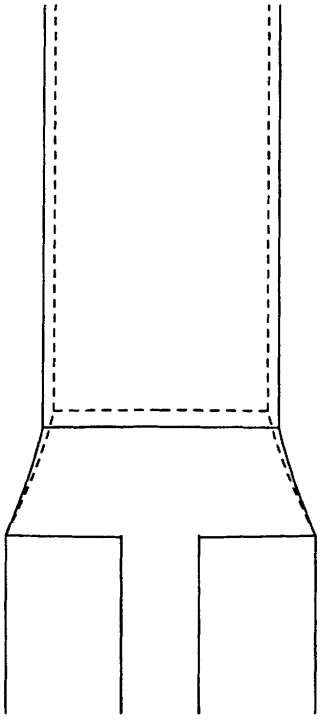

Figure 11. EFG system shapes for fiber pull rates (solid) $\hat{V} =$ $0{\cdot}0015\,\mathrm{cm\,s^{-1}}$ and (dashed) $\hat{V} =$ $0{\cdot}0085\,\mathrm{cm\,s^{-1}}$.

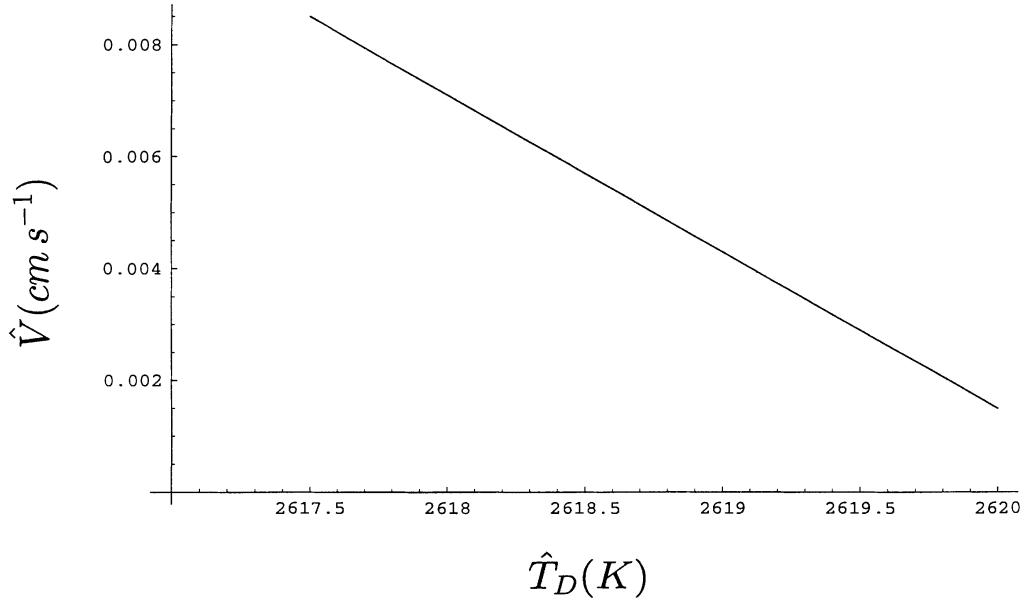

Figure 12. Operating points to produce a fiber with $\hat{F} = 0{\cdot}00609$ cm.

varies with the mean height H^* of the melt column. As the height increases, the contact angle decreases and F decreases to compensate. Thus, for a given die geometry and hydrostatic pressure, the magnitude of F is controlled by the input-die-melt temperature and pull velocity in this processing configuration.

Figures 9, 10, and 11 illustrate there dependencies. The results in Figures 10 and 11 suggest that to maintain a constant fiber radius while increasing pull velocity, one must lower the die temperature. The line in Figure 12 represents the pull velocity and die temperature needed to produce a fiber with the given constant radius. If one operates above (below) the line, then the fiber radius decreases (increases).

6. Summary

We have presented an axisymmetric model of the edge-defined film-fed growth process. This model describes steady-state heat transfer within the system. Our calculations involve a coupled asymptotic/numerical method. The method is based upon the following assumptions: small slenderness ratio (fiber radius/melt height), small surface heat transfer, and a melt column which is nearly a right circular cylinder. The advantage of the solution procedure is that it reduces the coupled set of partial differential equations to a simpler set which is easier to deal with numerically. We determine the solidifying and melt/gas interfacial shapes consistent with the system heat transfer and operating parameters in the limit of the small slenderness ratio ε. Liang and Shyy [7] and Shyy, Liang, and Wei [8] present a system for which ε appears to be slightly less than one. They calculate isotherms which appear to be parabolic in profile and relatively flat, indicating small radial thermal gradients. Our analysis is in agreement with these results. Further, the shape of the solidifying front, which we predict, also agrees with the concavity of this front in these same numerical simulations.

The intent of this work is to understand parametric dependencies within the EFG system. The results derived here can serve as initial data for a time-dependent model. Specifically, we have systematically derived one-dimensional equations for the temperature profiles and indicated the range of validity of these equations. We have shown that the temperature, pull velocity, and pressure determine the size of the fiber radius in the processing configuration driven by capillary action. Furthermore, an increase in the die temperature, or an increase in the pulling velocity of the fiber, or a decrease in the volumetric flow rate of the input melt (or pressure) causes the height of the melt region to increase.

Acknowledgement

This work was supported by NASA Grant NCC-3-104, NSF Grant DMS-95-32021, and an IBM RISC SYSTEM/6000 equipment grant.

References

1. D. G. Backman, D. Wei, L. C. Filler, R. Irwin and J. Collins, Modelling of the sapphire fiber growth process. In: E. F. Matthys and B. Kushner (eds), *Advanced Sensing, Modelling and Control of Materials Processing*. Warrendale, PA: The Minerals, Metals and Materials Society (1992) 3–17.
2. Y. A. Tatarchenko, *Shaped Crystal Growth, Fluid Mechanics and its Applications* vol. 20, Dordrecht: Kluwer Academic Publishers (1992) 287pp.
3. H. E. Labelle, A. I. Mlavsky and B. Chalmers, Growth of controlled profile crystals from the melt: Part I – Sapphire filaments. *Mater. Res. Bull.* 6 (1971) 571–580.
4. T. F. Ciszek, Edge-defined, film-fed growth (EFG) of silicon ribbons. *Mater. Res. Bull.* 7 (1972) 731–738.

5. T. F. Ciszek, Techniques for the growth of silicon ingots and ribbons. *J. Cryst. Growth* 66 (1984) 655–672.
6. T. Mah, T. A. Parthasarathy and L. Matson, Processing and properties of Al203/Y3Al5012 (YAG) eutectic composites. *Ceram. Eng. Sci. Proc.* 11 (1990) 1617–1627.
7. S-J. Liang and W. Shyy, Dynamic simulation of thin fibre growth. *J. Mat. Proc. and Manuf. Science* 2 (1993) 189–215.
8. W. Shyy, S-J. Liang, and D. Wei, Effect of dynamic perturbation and contact condition on edge-defined fiber growth characteristics. *Int. J. Heat and Mass Transfer* 37 (1994) 977–987.
9. H. M. Ettouney, R. A. Brown and J. P. Kalejs, Analysis of operating limits in edge-defined film-fed crystal growth. *J. Cryst. Growth* 62 (1983) 230–246.
10. H. M. Ettouney and R. A. Brown, Mechanisms for lateral solute segregation in edge-defined film-fed crystal growth. *J. Appl. Phys.* 55 (1984) 4384–4391.
11. H. K. Kuiken and P. J. Roksnoer, Analysis of the temperature distribution in FZ silicon crystals. *J. Cryst. Growth* 47 (1979) 29–42.
12. H. K. Kuiken, The cooling of low-heat-resistance cylinders by radiation. *J. Engng. Math.* 13 (1979) 97–106.
13. J. L. Duranceau and R. A. Brown, Thermal-capillary analysis of small-scale floating zones: steady-state calculation. *J. Cryst. Growth* 75 (1986) 367–389.
14. G. W. Young A. and Chait, Steady-state thermal-solutal diffusion in a float zone. *J. Cryst. Growth* 96 (1989) 65–95.
15. G. W. Young A. and Chait, Surface tension driven heat, mass, and momentum transport in a two-dimensional float zone. *J. Cryst. Growth* 106 (1990) 445–466.
16. C. W. Lan and S. J. Kou, Floating-zone crystal growth with a heated ring covering the melt surface. *J. Cryst. Growth* 108 (1991) 1–7.
17. C. W. Lan and S. J. Kou, Floating-zone crystal growth with a heated and immersed shaper computer simulation. *J. Cryst. Growth* 108 (1991) 340–350.
18. K. Brattkus and S. H. Davis, Directional solidification with heat losses. *J. Cryst. Growth* 91 (1988) 538–556.
19. J. A. F. Plateau. In: *Statique Experimentale et Theorique des Liquides Soumis aux Seules Forces Moleculaires*. Paris: Gauthier-Villars (1873).
20. Lord Rayleigh, On the capillary phenomena of jets. *Proc. R. Soc. of London* 29 (1879) 71–97.
21. V. W. Heywang and G. Ziegler, Zur Stabilitat senkrechter Schmelzzonen. *Zeit. für Naturforschung. A* 9A (1954) 561–562.
22. V. W. Heywang, Zur Stabilïtat senkrechter Schmelzzonen. *Zeit. für Naturforschung. A* 11A (1956) 238–243.
23. S. R. Coriell, S. C. Hardy and M. R. Cordes, Stability of liquid zones. *J. Colloid and Interf. Sci.* 60 (1977) 126–136.
24. T. Surek and S. R. Coriell, Shape stability in float zoning of silicon crystals. *J. Cryst. Growth* 37 (1977) 253–271.
25. E. M. Sachs and T. Surek, Dynamics and control of meniscus height in ribbon growth by the EFG method. *J. Cryst. Growth* 50 (1980) 114–125.
26. V. A. Tatarchenko and E. A. Brener, Crystallization stability during capillary shaping. *J. Cryst. Growth* 50 (1980) 33-44.
27. M. A. Matovich and J. R. A. Pearson, Spinning a molten threadline. *Ind. Eng. Chem. Fundam.* 8 (1969) 512–520.
28. F. T. Geyling, Basic fluid-dynamic considerations in the drawing of optical fibers. *Bell Syst. Tech. J.* 55 (1976) 1011–1056.
29. W. W. Schultz and S. H. Davis, One-dimensional liquid fibers. *J. Rheol.* 26 (1982) 331–345.
30. J. N. Dewynne, J. R. Ockendon and P. Wilmott, A systematic derivation of the leading-order equations for extensional flows in slender geometries. *J. Fluid Mech.* 244 (1992) 323–338.
31. L. R. Glicksman, The dynamics of a heated free jet of variable viscosity liquid at low Reynolds numbers. *J. Basic Eng., Trans. ASME* 90 (1968) 343–354.
32. U. C. Paek and R. B. Runk, Physical behavior of the neck-down region during furnace drawing of silica fibers. *J. Appl. Phys.* 49 (1978) 4417–4422.
33. M. R. Myers, A model for unsteady analysis of preform drawing. *AIChE J.* 35 (1989) 592–602.
34. G. Gupta and W. W. Schultz, Non-isothermal flows of Newtonian slender glass fibers. *Int. J. Non-Lin. Mech.* 33 (1998) 151–163.
35. A. Oron, S. H. Davis and S. G. Bankoff, Long-scale evolution of thin liquid films. *Rev. Mod. Phys.* 69 (1997) 931–980.